LASER & PHOTONICS REVIEWS
www.lpr-journal.org

Large Beam Size Grating Coupler in Silicon-on-Insulator Using Fully Etched Subwavelength Gratings

Miguel Barona-Ruiz, Laureano Moreno-Pozas, Pablo Ginel-Moreno, Alejandro Ortega-Moñux, José de Oliva-Rubio, Íñigo Molina-Fernández, J. Gonzalo Wangüemert-Pérez, and Robert Halir*

Several emerging applications of silicon photonics, including sensing, ranging, and optical trapping, require fixed, well-collimated beams that enable interaction with targets placed centimeters away from the chip. Generating such beams without using bulk-optic lenses entails radiating lightwaves with diameters of hundreds of microns directly from the chip. Gratings with sufficiently low strength have so far only been shown in the silicon nitride platform using specialized shallow etch steps; in silicon-on-insulator the implementation becomes much more challenging due to the increased index contrast. Here, the first silicon-on-insulator grating capable of radiating such large beams is reported. Using a fully etched, double-period subwavelength structure, with feature sizes compatible with deep-ultraviolet lithography, a beam diameter in excess of 350 µm, with a 54% radiation efficiency, is experimentally demonstrated.

1. Introduction

Silicon photonics is enabling the miniaturization of complex optical systems in integrated optical chips that can be fabricated at scale.[1–3] Driven by its success in Telecom and Datacom, this technology is rapidly expanding into new areas such as biosensing,[4,5] optical coherence tomography,[6] coherent imaging,[7] light detection and ranging (LIDAR),[8] or optical trapping.[9] Miniaturization does, however, come at a price: interfacing silicon chips with the outside world is a challenge, due to the extremely small size of the waveguides, of the order of 220 × 500 nm. For telecom and datacom, efficient coupling from these waveguides to standard optical fibers placed in close proximity to the chip is key. This can be achieved with inverse tapers[10] or conventional grating couplers that generate fixed off-chip beams with a diameter of 10 µm.[11] For other application areas the interfacing requirements are rather different. For LIDAR, steerable beams with very small divergence are needed.[12,13] These can be generated with optical phased arrays (OPAs): periodic arrangements of optical antennas fed through a phase-tunable network of waveguides. However, the periodic spacing of the antennas also causes side-lobes in the radiated field, and, conversely, limits their collecting efficiency since light that impinges between the antennas is not coupled into the chip. Many other applications, including imaging and ranging sensors,[7,14] optical trapping,[9] and cardiovascular sensors,[15] require one or several fixed, well-collimated optical beams to enable interaction with targets situated at centimeter-scale distances from the chip. For these applications a combination of conventional grating couplers and bulk-optics lenses is often employed. However, such opto-mechanical solutions are bulky and require careful alignment, thus eroding some of the advantages of optical integration.

Consequently there has been a growing interest in grating couplers that can generate beams with diameters in the range of hundreds of microns without requiring any tuning: such beams exhibit centimeter-scale Rayleigh distances and are thus well suited for direct, lens-less interactions between photonic chips and macroscopic targets.[9,16–24] These grating couplers are usually implemented via the combination of a mode transformer that expands the beam in the lateral direction and a weak grating that radiates the beam with the desired longitudinal profile, as shown schematically in **Figure 1**a,b. The lateral mode expansion is readily achieved using evanescent coupling or sidewall deflectors.[17,25] For the grating coupler, the challenge lies in achieving a weak, yet well-controlled radiation strength. In the silicon-nitride platform this can be achieved with an additional shallow etch depth, or a polymer overlay, yielding mode field diameters of ≈ 300 µm.[9,17,19–21,23,24] However, these additional fabrication steps add complexity and cost. Some single-etch

M. Barona-Ruiz, L. Moreno-Pozas, A. Ortega-Moñux, J. de Oliva-Rubio, Í. Molina-Fernández, J. G. Wangüemert-Pérez, R. Halir
Telecommunication Research Institute (TELMA)
Universidad de Málaga
CEI Andalucía TECH
Louis Pasteur 35, Málaga 29010, Spain
E-mail: miguelbr@uma.es
P. Ginel-Moreno
AGPHOTONICS, Edf. Bioinnovación UMA
C. Severo Ochoa, 34, Málaga 29590, Spain

The ORCID identification number(s) for the author(s) of this article can be found under https://doi.org/10.1002/lpor.202401775

DOI: 10.1002/lpor.202401775

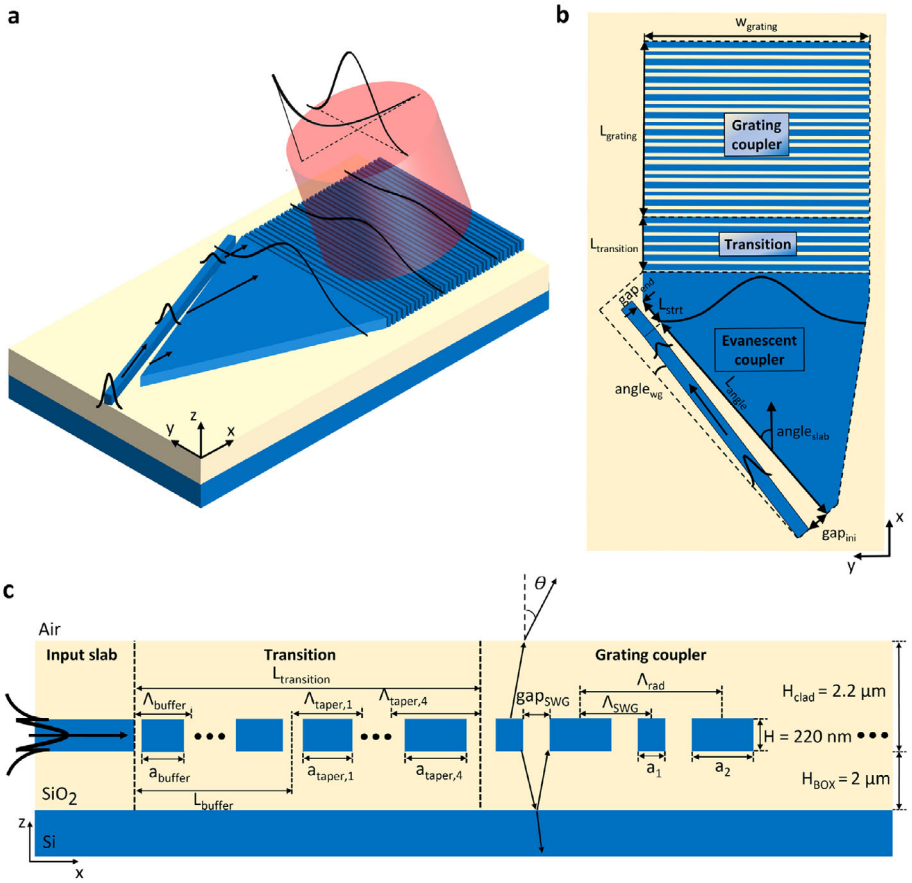

Figure 1. Diagrams of the proposed device. The diagrams are not to scale. a) 3D Schematic of the device operation. SiO_2 upper cladding not shown for clarity. b) Schematic top-view of the complete device. c) Side diagram of the transition and the grating coupler.

step designs have been demonstrated in silicon nitride at the expense of requiring precise control over feature size and shape.[22] Designing such gratings in the more commonly used silicon-on-insulator platform is far more challenging, since it exhibits a much stronger index contrast than the silicon nitride platform, creating intrinsically stronger scattering. Indeed, the literature on large grating couplers in silicon-on-insulator is scarce: a modest-size 100 µm mode field diameter) grating based on a customized two etch-step process is demonstrated in [18].

Here, we propose and experimentally demonstrate what is, to the best of our knowledge, the first large-area grating coupler that can be fabricated in a single, full etch step in the silicon-on-insulator platform. Leveraging the properties of subwavelength structures,[26,27] we design a grating with a longitudinal mode field diameter of 450 µm (350 µm measured experimentally), corresponding to a Rayleigh length of 10.2 cm (6.2 cm). Comparably large feature sizes of 126 nm ensure that the device is also fabricable at scale.

2. Device Structure and Operation Principle

Our grating design is shown schematically in Figure 1a,b and consists of three distinct regions:

- An evanescent coupler to expand the mode from the single-mode waveguide to a 100 µm mode field diameter (MFD) gaussian slab mode. We used this intermediate width to save chip area and note that using the same principle wider slab modes can be readily generated.
- A transition region that provides gradual matching between the large slab region and the diffractive grating itself. This transition reduces back-reflections, and facilitates homogeneous etching conditions along the grating.
- The diffractive grating itself, which radiates light with a longitudinal mode field diameter of 450 µm. The key to achieving this remarkable beam size with fully etched silicon waveguides is illustrated in Figure 1c: each radiation period, Λ_{rad}, is divided into two subwavelength segments spaced at $\Lambda_{SWG} = \Lambda_{rad}/2$. When the subwavelength segments are identical in size, i.e., $|a_2 - a_1| = 0$, the structure acts as an equivalent homogeneous waveguide, suppressing all diffraction effects.[26,27] When $|a_2 - a_1| > 0$ the structure starts diffracting, and the amount of light that is coupled into freespace in each radiation period is directly controlled by the difference in segment size, $a_2 - a_1$, enabling extremely large beam sizes, as described in detail in Section 3.3. While most grating topologies require smaller feature sizes to achieve larger beam sizes, our approach works with comparatively large segments with small size differences, making it more amenable to fabrication.

Table 1. Optimized parameters of the 450 µm MFD grating coupler shown in Figure 1. Note that the gaps in the buffer region are simply given by $\Lambda_{buffer} - a_{buffer}$.

Gap_{ini}	Gap_{end}	$Angle_{wg}$	L_{angle}	L_{strt}	$Angle_{slab}$	$w_{grating}$	$L_{grating}$
1360 nm	200 nm	0.135°	495.5 µm	40 µm	30.3°	340 µm	950 µm
L_{buffer}	Λ_{buffer}	a_{buffer}	$\Lambda_{taper,1}$	$a_{taper,1}$	$\Lambda_{taper,2}$	$a_{taper,2}$	$\Lambda_{taper,3}$
50 µm	320 nm	224 nm	352 nm	246 nm	384 nm	269 nm	416 nm
$a_{taper,3}$	$\Lambda_{taper,4}$	$a_{taper,4}$	Λ_{SWG}	a_1	a_2	gap_{SWG}	
291 nm	450 nm	315 nm	450 nm	126 nm	247.5 nm	263.25 nm	

For our design, we consider a 220 nm thick silicon on insulator platform, surrounded by a 2 µm and 2.2 µm thick buried silica layer and cladding, respectively. The operation wavelength is 1.55 µm and transverse magentic-polarized (TM-polarized) light is assumed. As a proof of principle, we will focus here on an unapodized design with an equivalent MFD of 450 µm. Since beams with an exponentially decaying field profile, $\exp(-\alpha x)$, and radiating at an angle θ, can be well approximated by a gaussian beam with mode field diameter[28]

$$\mathrm{MFD} = 1.36\cos(\theta)/\alpha \quad (1)$$

this corresponds to a field decay factor $\alpha = 3\,\mathrm{Npmm}^{-1}$. Indeed, we will show below that the far-field of this exponential near-field beam is almost indistinguishable from the far-field of a gaussian beam with a MFD of 450 µm.

3. Design

3.1. Evanescent Coupler

To feed the grating coupler with the required profile, an evanescent coupler is designed, as shown schematically in Figure 1b. It converts the 500 nm-wide waveguide mode into a quasi-gaussian slab-guided wave with a 100 µm mode-field diameter and a flat wavefront, parallel to the grating. This wave is radiated within the chip plan at an angle of $angle_{slab} = 30.3°$ with respect to the waveguide. The shape of the radiated wave is controlled by the gap between the input waveguide and the slab: with an initial gap of 1360 nm, the waveguide approaches the silicon slab with an angle of $angle_{wg} = 0.135°$ along a length of $L_{angle} = 495.5$ µm, when the gap between the waveguide and the slab is $gap_{end} = 200$ nm. Then, the approaching waveguide is set parallel to the slab over the remaining length $L_{strt} = 40$ µm. The optimized geometric parameters of the coupler are given in **Table 1**.

3.2. Transition Region

To reduce spurious reflections from the grating region, we designed a ≈ 50 µm long transition region between the evanescent coupler and the grating. As shown in Figure 1b, this region consists of a subwavelength grating (SWG) with period $\Lambda_{buffer} = 320$ nm and duty cycle $DC_{buffer} = a_{buffer}/\Lambda_{buffer} = 0.7$ that maintains low reflections and suppresses diffraction, even when over or under-etched. Then, four periods are added so that the pitch Λ_{taper} of the structure is linearly tapered from $\Lambda_{buffer} = 320$ nm to $\Lambda_{SWG} = 450$ nm, matching the pitch of the grating. Indeed, in our design this approach yields back reflections below −14 dB. The exact dimensions used in the transition region are summarized in Table 1. We note that the dimensions in this region are not critical as long as they provide a smooth transition between the waveguide and the grating itself, and that back-reflections could be further reduced by using the transition to not only match the pitch but also the duty-cycle of the grating. A further advantage of the transition region is that it alleviates the abrupt change in feature density between the grating coupler and the large input slab that poses a challenge for some fabrication processes.

3.3. Diffractive Grating

The grating's main feature is the use of a radiation period Λ_{rad} composed of two subwavelength periods: $\Lambda_{rad} = 2\Lambda_{SWG}$, as shown in Figure 1c. We define the duty cycle of both periods as $DC_1 = a_1/\Lambda_{SWG}$ and $DC_2 = a_2/\Lambda_{SWG}$. The grating only radiates light when the duty cycle difference $\Delta DC = DC_2 - DC_1$ is nonzero, enabling us to control the radiation strength in a wide margin.

To study the behavior of the grating we used an in-house Bloch–Floquet mode solver (FEXEN).[29] The grating operation depends mainly on three parameters: the pitch of the radiation period Λ_{rad}, the mean duty cycle of both periods $DC_{mean} = (DC_1 + DC_2)/2$, and the difference between the duty cycles of both SWG periods, ΔDC. In the following we will derive a procedure to select these three parameters in order to obtain a desired radiation angle (θ) and mode field diameter (MFD).

Our approach is based on the fact that the radiation angle depends only weakly on the difference of duty cycles, ΔDC. This can be understood by examining the grating equation in the first radiation zone, $\theta = \arcsin(n_B - \lambda/\Lambda_{rad})$, where n_B is the effective index of the Bloch mode of the grating, λ is the working wavelength and θ is the radiation angle. It is clear that the angle depends on Λ_{rad} and n_B. Intuitively, if ΔDC is changed, but DC_{mean} is kept constant, the effective index of the mode n_B will change only slightly, since the amount of silicon in the radiation period remains the same; thus the radiation angle will not change. This is can be verified in **Figure 2a,b**, which show simulated countour maps of the radiation angle as a function of ΔDC, DC_{mean}, and Λ_{rad}. It can be observed that the contour lines are almost vertical until the Bragg zone is reached, indicating that the angle is indeed almost independent of ΔDC in the first radiation zone.

We can now conveniently represent the radiation angle θ as function of only DC_{mean} and Λ_{rad}, as shown in **Figure 3a**, for $\Delta DC = 0.27$. The contour lines allow us to find different design points $\{\Lambda_{rad}, DC_{mean}\}$ for the desired θ. We consider $\theta = -8.5°$ as target angle, since it is close to vertical radiation, but with a safe margin to the Bragg regime. Three points that achieve $\theta = -8.5°$ are marked in Figure 3a: $\Lambda_{rad} = 860$ nm, $DC_{mean} = 0.59$; $\Lambda_{rad} = 880$ nm, $DC_{mean} = 0.51$; $\Lambda_{rad} = 900$ nm, $DC_{mean} = 0.415$.

To determine which one of these points is best suited for our target mode field diameter, we analyse the Floquet mode field decay factor α as a function of ΔDC, yielding the results shown in Figure 3b. We observe that the radiation strength grows approximately as a fourth order polynomial with ΔDC, and, critically,

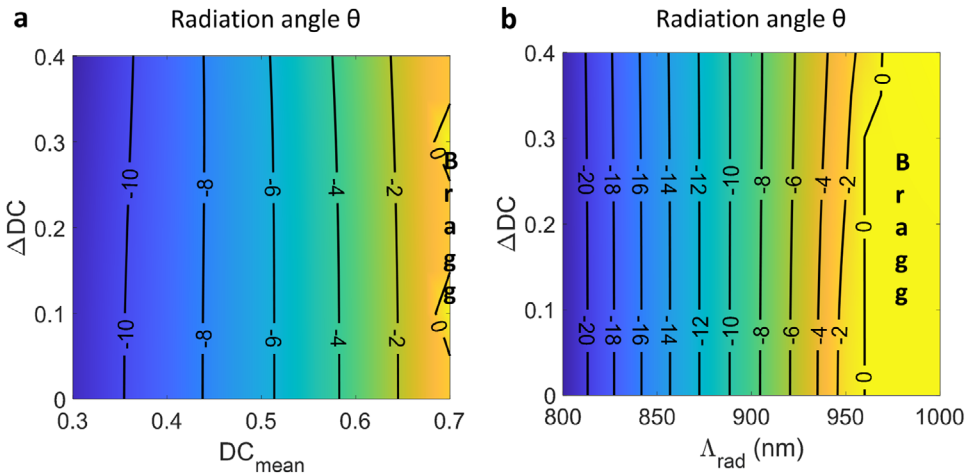

Figure 2. Contour map of the radiation angle θ a) as a function of DC_{mean} and ΔDC for $\Lambda_{rad} = 900$ nm, and b) as a function of Λ_{rad} and ΔDC for $DC_{mean} = 0.44$. In both cases the radiation angle is virtually independent of ΔDC.

arbitrarily small values of α, and hence very large mode field diameters, can be achieved by simply reducing ΔDC. The rate of change of α depends mainly on the DC_{mean} at each design point. The figure also shows how the angle θ changes at maximum 0.5° in the entire sweep, which makes it particulary straightforward to apodize the grating if needed. We now simply select the point in each curve that achieves the desired radiation strength α. In our case, the radiation strength that achieves an equivalent MFD of 450 µm is $\alpha = 3\ \mathrm{Npmm^{-1}}$ (see Equation (1)).

In Figure 3c, the parameters for designs A, B, and C are shown, along their respective radiation efficiency (RE), i.e., the amount of power radiated upwards (into air). The RE was calculated by placing a power monitor at a height of 5.5 µm above the grating, in the air region. The power measured by the power monitor in the upward direction is divided by the total power injected into the grating to obtain the RE. The RE is dependent on the radiation angle and the BOX thickness (2 µm in this platform), since it depends on the interference produced by the beam that is radiated upwards and the beam that is radiated downwards and then reflected at the BOX-substrate interface (see Figure 1c). The layer thicknesses considered for these simulations are given in Figure 1c. Since the RE does not vary significantly between the different points, we can choose the design point based on tolerances to fabrication errors and the minimum feature size. We

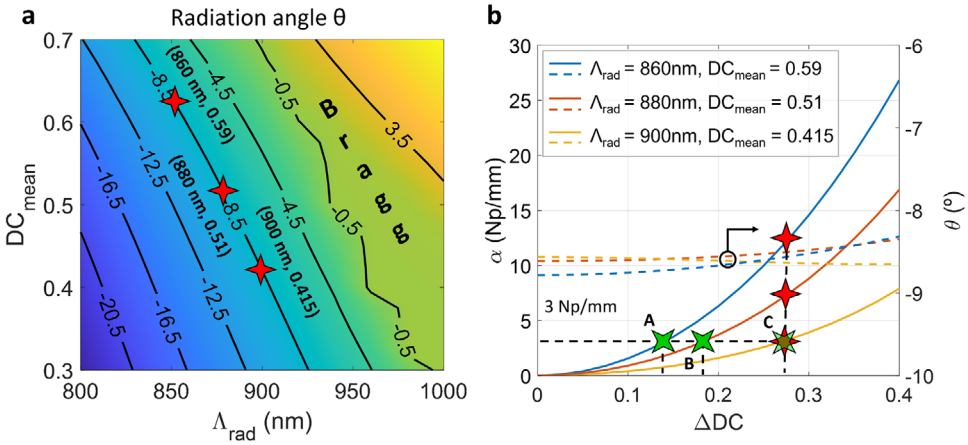

c

	Λ_{rad} (nm)	DC_{mean}	ΔDC	RE (%)
Design A	860	0.59	0.14	59
Design B	880	0.51	0.18	60
Design C	900	0.415	0.27	61

Figure 3. a) Contour map of θ as a function of Λ_{rad} and DC_{mean}, for a ΔDC of 0.27. The three red stars mark three different combinations of (Λ_{rad}, DC_{mean}) that result in $\theta = -8.5°$. b) ΔDC sweep of the radiation strength α (left axis) and radiation angle θ (right axis) for the three points previously chosen in Figure 3a, marked with red stars. The three green stars mark the points of each curve where $\alpha = 3\ \mathrm{Npmm^{-1}}$, equivalent to the desired MFD of 450 µm. c) Parameters of the three designed gratings, where the radiation efficiency (RE) is the fraction of input power radiated upwards.

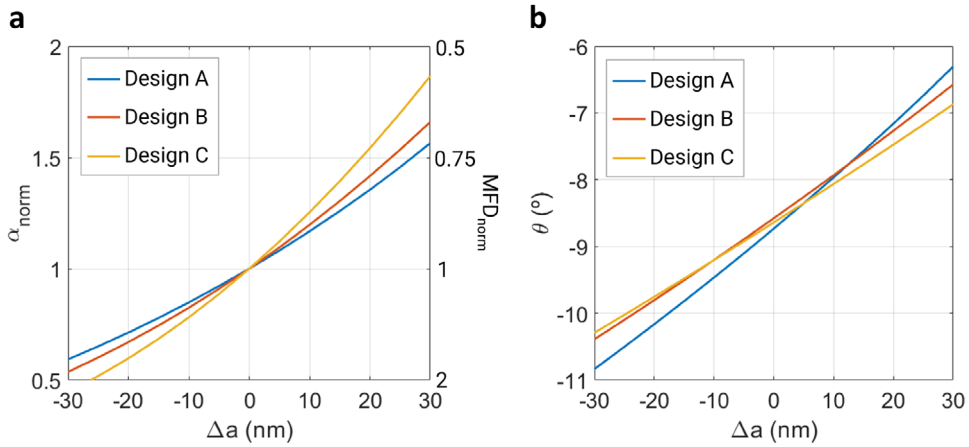

Figure 4. Fabrication tolerances for a) the normalized radiation strength α and b) the radiation angle θ at the three points chosen in Figure 3b, for a fabrication error up to 30 nm. α_{norm} is defined as $\alpha_{norm} = \alpha(\Delta a)/\alpha(\Delta a = 0\,\text{nm})$.

note that by using a second etch depth one could create a vertical asymmetry that can contribute to an enhanced radiation efficiency. This would also further weaken the perturbation, enabling even larger beam sizes. The tolerance analysis for the radiation strength α and radiation angle θ is presented in **Figure 4**a,b, respectively, where a_1 and a_2 (see Figure 1a) are increased or decreased by Δa, resulting in $a_1' = a_1 + \Delta a$ and $a_2' = a_2 + \Delta a$. For a ±30 nm error the radiation strength increases or decreases approximately by a factor of 1.5 to 1.8. On the other hand, for the same fabrication deviation a ±2° error in the radiation angle θ occurs. Regarding changes in temperature, we have checked that the performance of the gratings barely changes even with changes in excess of 50°.

For our design we choose point C, where $\Lambda_{rad} = 900$ nm, $DC_{rad} = 0.415$ and $\Delta DC = 0.27$, since this is the point with less angle variations due to fabrication errors. The width of the grating $w_{grating} = 340\,\mu$m, is chosen so that the slab mode produced by the evanescent coupler is confined within the grating coupler. Likewise, we select the length of the grating for it to radiate most of the input power, $L_{grating} = 950\,\mu$m. The complete design parameters can be found in Table 1. We note that while our smallest feature size is 96 nm in the buffer region, the grating works with features larger than 120 nm, and could be further optimized to be fully compatible with DUV lithography. To check the performance of the designed grating, the fundamental TM mode propagation along the grating is simulated using FEXEN as shown in **Figure 5**a. Once the radiated field is obtained, the radiation diagram is calculated from the near-field, following the method outlined in [30] section 2.3.1, yielding the results shown in Figure 5b. We observe that the center of the radiation diagram is $\theta = -8.5°$ and the full width at the half maximum power for the elevation axis ($FWHM_\theta$) is 0.1°. This matches well with the theoretical value of $FWHM_\theta = 0.09°$ for an exponential with $\alpha = 3\text{Npmm}^{-1}$ obtained via[31]:

$$\text{FWHM}_\theta = \frac{2\alpha}{k_0 \cos\theta} \tag{2}$$

Referring to Figure 5b we note that while the far-field of our grating does not exhibit exactly the same shape as that of a gaussian with MFD = 450 µm (the overlap value between them is 77%), their $FWHM_\theta$ values are very similar. This validates our approach to generate beams for lens-less interaction at centimeter scales. We additionally note that by using a second etch depth

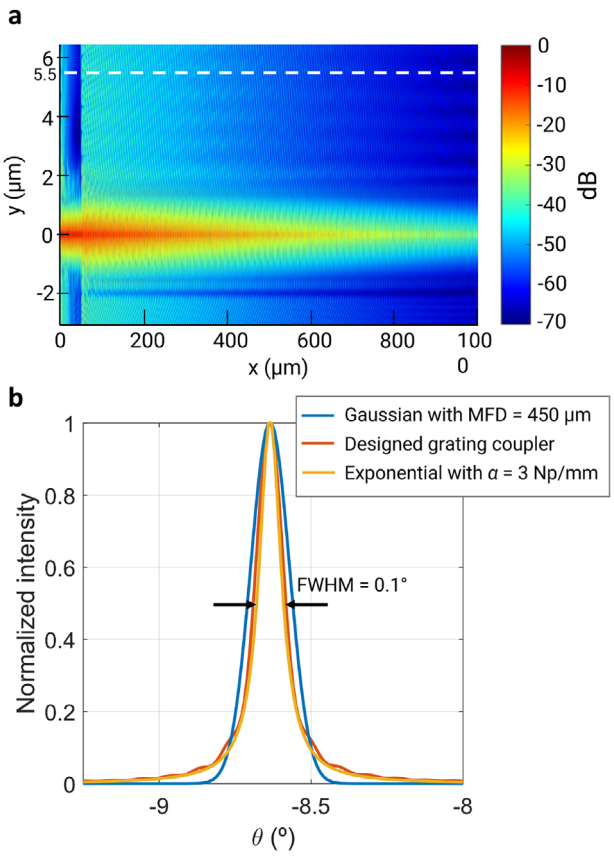

Figure 5. a) Field propagation along the grating, in a logarithmical scale. The near-field is monitored along the dashed white line. Note that the transition region extends along first 50 µm. b) Calculated far-field diagram of the designed grating, compared to the radiation diagram of a 450 µm theoretical gaussian and of an exponential with $\alpha = 3\,\text{Npmm}^{-1}$.

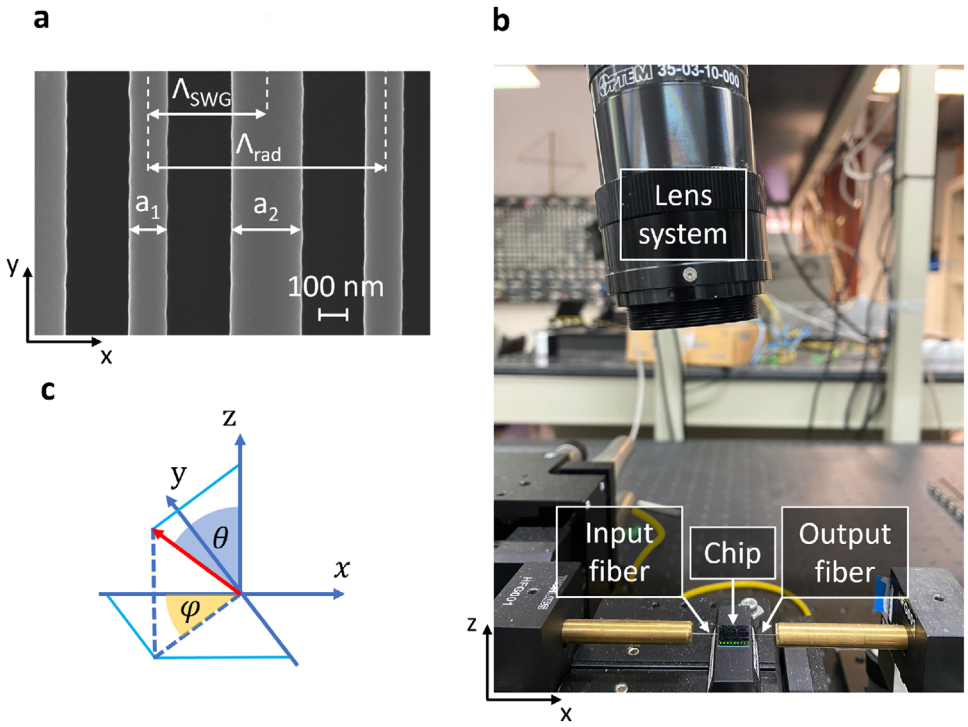

Figure 6. a) SEM image of part of the grating coupler showing the grating period and the subwavelength period. b) Photograph of the setup used to measure the grating coupler. c) Coordinate system used for the measurements.

one could create a vertical asymmetry that can contribute to an enhanced radiation efficiency. This would also further weaken the perturbation, enabling even larger beam sizes.

4. Experimental Results

To experimentally validate our design, the grating coupler was fabricated using Applied Nanotool's standard single-etch process for 220 nm SOI, with a 2 µm thick buried oxide layer.[32] A 100 keV electron-beam was used to pattern the resist, and structures were transferred into the silicon layer via reactive ion etching. A 2.2 µm-thick oxide layer was deposited on top using plasma enhanced chemical vapor deposition. This technique is known to produce small air gaps when filling narrow trenches. However, our simulations showed that these gaps do not have a significant impact on the performance of the grating. A SEM image of the grating coupler is shown in **Figure 6**a, showing a good reproduction of the grating structure, with minor roughness on the edges.

To measure the grating coupler, the setup shown in Figure 6b is used. An Agilent 8164B lightwave measurement system is employed, equipped with a 81600B tunable laser output and a 81634B power sensor. A polarization rotator is connected to the laser output to set the desired polarization at the chip input. Lensed fibers are used to inject the light in and out of the chip's edges, with spot size converters placed at the edge of the chip to improve the coupling between the lensed fibers modes and the on-chip waveguides.[10] The coordinate system used for the measurements is illustrated in Figure 6c, where x is the direction of propagation of light within the chip.

On the chip, light is split evenly into two waveguides. The first waveguide serves as a reference directing light to the output lensed fiber connected to the 81634B power sensor. The second waveguide is directly connected to the grating. In order to measure the light radiated by the grating coupler, the WiDy SenS 640V-ST IR camera is used with either a near-field or far-field lens system. To measure the near-field, we used a lens system composed of the Excelitas 45-08-06-000 x1 camera tube, the 45-31-10-000 7:1 zoom module and the 35-03-10-000 15 mm manual focus element. The camera was placed perpendicular to the beam, at the expected angle of $\theta = -8.5°$. The working distance of the lens system is 20 cm and known physical distances on the chip were used to calibrate the axes measured with the camera.

The resulting near-field measurements are shown in **Figure 7**a. Along the transversal y-axis, the field expanded by the evanescent coupler is quasi-gaussian with a MFD = 120 µm. This reasonably matches the designed value of 100 µm. Figure 7c shows the longitudinal x-axis cut at the point of maximum power, as well as a fit with an exponential curve with $2\alpha = 7.6\ \mathrm{Npmm^{-1}}$. This corresponds, following Equation (1), to an equivalent MFD of 358 µm and is close to the designed value of $2\alpha = 6\ \mathrm{Npmm^{-1}}$. This experimentally validates our design approach to achieve large mode field diameters with fully etched gratings in silicon.

Next, we designed a far-field lens system that transforms angles into displacements in the focal plane, i.e., the camera sensor; this displacement depends on the focal length (f) of the lens: $d = \tan(\text{angle}) \times f$. The designed lens system consists of an Thorlabs AC254-030-C-ML lens, an SM1L03 lens tube and the SM1A9 adapter for the camera. The camera sensor has a width and height of 9.6 mm × 7.68 mm, while the lens has a focal length

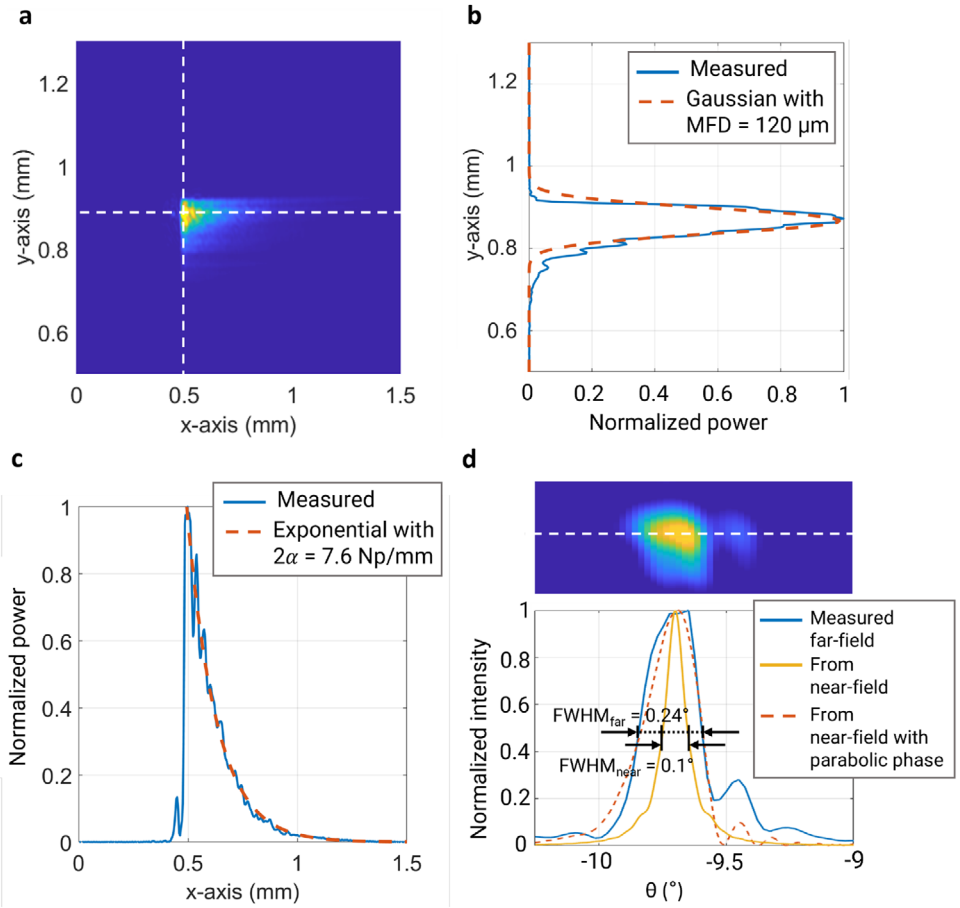

Figure 7. a) Measured near-field power radiated by the grating coupler. Cut at position of maximum power along b) the *y*- axis and c) the *x*-axis. d) Measured far-field intensity and cut along the θ-axis, compared with the radiation diagram calculated from the near-field measurement with linear phase and parabolic phase.

of 35.1 mm. Therefore, the field of view of the system for the elevation angle is $\frac{180°}{\pi} \times \frac{9.6}{35.1} = 15.7°$; while the azimuth field of view is $\frac{180°}{\pi} \times \frac{7.68}{35.1} = 12.5°$. Since the camera has 640×512 pixels, the system has a resolution of 0.025°. We use the far-field lens system to measure both θ and ϕ, rotating the camera until it is completely perpendicular to the beam.

The measured far-field radiation is represented in Figure 7d, along an elevation axis (θ) cut at the point of maximum intensity. There is a small shift in the elevation angle from the designed value of −8.5° to −9.6° in the measurements. The full width at half maximum ($FWHM_\theta$) is 0.24°, which is broader than the 0.1° expected from Figure 5b. To investigate this discrepancy, we calculated the far-field intensity from the measured near-field using the same method as in the design section, and assuming a perfectly linear phase. As shown in Figure 7d, this yielded a $FWHM_\theta$ of 0.11° closely matching the theoretical value. This suggests that the broadening arises from minor fabrication imperfections that result in a slighly non-linear phase. Indeed, calculating the far field intensity from the measure near field, with an added parabolic phase $15x^2$ [rad] centered at the beginning of the grating, yields a very good fit with the directly measured far field, as shown in Figure 7d. Such a parabolic phase error could arise, for example, from spurious chirping of the grating period of the order of 4 nm mm^{-1} along the grating.

To measure the radiation efficiency of the grating we proceeded as follows. First, the camera with the far-field lens system was power-calibrated, using a collimated beam with known power-levels and ensuring that the non of the pixels of the camera saturated. A sequence of frames of the light radiated by the grating was then recorded. To reduce noise, 15 frames were averaged, and the dark-frame was substracted. The total radiated power was then obtained by adding the value of all pixels. After a thorough calibration of the system losses, detailed in Appendix A, we obtained a radiation efficiency of the grating coupler of 54 %, close to the simulated value of 64 %.

Table 2 summarizes our results compared to existing literature. We highlight that most designs are reported for the silicon nitride platform and use two etch steps. Compared to the only work reported so far in silicon-on-insulator our approach provides a more than threefold increase in beam diameter, and an enhanced radiation efficiency, while using only a single etch step. Regarding repeatability we measured a variety of other designs targeting MFDs ranging from 185 μm to 450 μm and measured deviations of less than 25% in MFD compared to the target values.

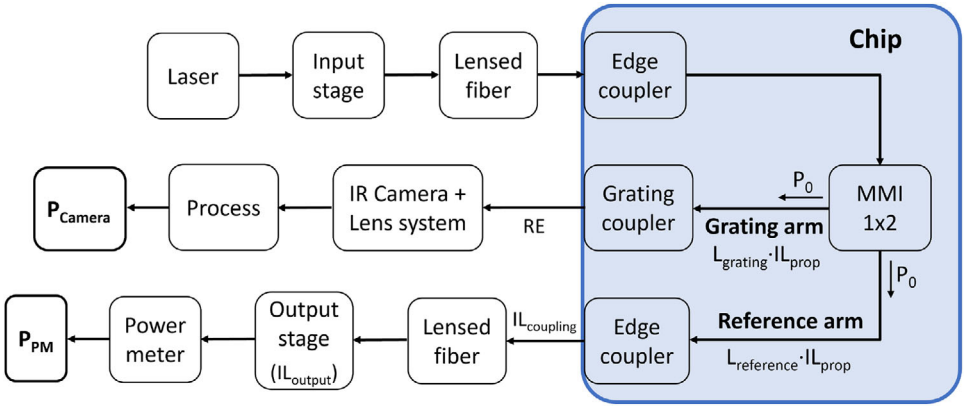

Figure A1. Schematic of the measurement system components and the in-chip components.

Table 2. Comparative table between previous works and our paper.

Paper	Platform	MFD [μm]	Radiation efficiency	Number of etch steps
[17]	SiN	320	67 %	Two
[9]	SiN	707	16 %	Two
[19]	SiN	200	56 %	Two
[20]	SiN	160	—	Two
[24]	SiN	160	70 %	Two
[21]*	SiN	80	7.9 %	Two
[22]	SiN	~ 200†	63 %	One
[18]	SOI	100	33 %	Two
This work	**SOI**	**358**	54 %	**One**

The work marked with * have not been experimentally characterized. † Indirect measurements of up to milimeter size diameters are also reported, but require sidewall corrugations of the order of a few nanometers.

5. Conclusions

We have proposed and demonstrated a novel grating structure capable of producing beams with diamaters of hundreds of microns in the silicon-on-insulator platform, thereby enabling efficient interactions with targets centimeters away from the chip. The judicious use of subwavelength structuring enables devices with DUV-compatible feature sizes that can be fabricated with a single etch step. Furthermore, the subwavelength topology can create a wide range of grating strength, making apodization straightforward. We believe that this approach will enable large scale fabrication of photonic far-field sensors.

Appendix A: Calculation of the Radiation Efficiency

Figure A1 shows the block diagram of the different components of the measurement setup and inside the chip. To characterize the radiation efficiency (RE) of the grating coupler we compare the power measured at the power meter, P_{PM}, and the camera, P_{Camera}. At the outputs of the 1×2 MMI power is split evenly towards the reference arm and the grating arm with power P_0. Within the reference arm losses arise from propagation through the waveguide, $IL_{prop} = 2.6\,dBcm^{-1}$ along a length of $L_{reference} = 0.5$ cm, coupling of the light between the edge coupler and the output lensed fiber $IL_{coupling} = 2.25$ dB, and fiber connectors of the output stage, $IL_{output} = 0.6$ dB. In the grating coupler arm, the losses are induced by the waveguide propagation IL_{prop} along a length of $L_{grating} = 0.06$ cm and by the radiation efficiency of the grating coupler. We can summarize the above with the following equation expressed in dB:

$$\text{Reference arm}: \; P_{PM} = P_0 - IL_{output} - IL_{coupling} - IL_{prop} L_{reference} \quad \text{(A1)}$$

$$\text{Grating arm}: \; P_{Camera} = P_0 + RE - IL_{prop} L_{grating} \quad \text{(A2)}$$

From these equations, we find the radiation efficiency as:

$$RE = P_{Camera} - P_{PM} - IL_{output} - IL_{coupling} - IL_{prop}(L_{reference} - L_{grating}) \quad \text{(A3)}$$

For a laser input power of −10 dBm, the measured power at the power meter was $P_{PM} = -24.4$ dBm and while the power measured with the camera was $P_{Camera} = -23.1$ dBm. By using the equation above, we obtain a radiation efficiency $RE = -2.7\,dB = 54\,\%$.

Acknowledgements

The authors acknowledge funding through project TED2021-130400B-I00/ AEI/10.13039/501100011033/ Unión Europea NextGenerationEU/PRTR and project PDC2023-145833-I00/ Ministerio de Ciencia, Innovación y Universidades and Funding for open access charge: Universidad de Malaga/CBUA.

Conflict of Interest

The authors declare no conflict of interest.

Data Availability Statement

The data that support the findings of this study are available from the corresponding author upon reasonable request.

Conflict of Interest

The authors declare no conflict of interest.

Keywords

collimated beams, free-space coupling, grating couplers, silicon photonics, subwavelength grating metamaterials

Received: October 23, 2024
Revised: February 3, 2025
Published online:

[1] X. Chen, M. M. Milosevic, S. Stanković, S. Reynolds, T. D. Bucio, K. Li, D. J. Thomson, F. Gardes, G. T. Reed, *Proc. IEEE* **2018**, *106*, 2101.
[2] S. Y. Siew, B. Li, F. Gao, H. Y. Zheng, W. Zhang, P. Guo, S. W. Xie, A. Song, B. Dong, L. W. Luo, C. Li, X. Luo, G.-Q. Lo, *J. Lightwave Technol.* **2021**, *39*, 4374.
[3] S. Shekhar, W. Bogaerts, L. Chrostowski, J. E. Bowers, M. Hochberg, R. Soref, B. J. Shastri, *Nat. Commun.* **2024**, *15*, 751.
[4] J. G. Wangüemert-Pérez, A. Hadij-ElHouati, A. Sánchez-Postigo, J. Leuermann, D.-X. Xu, P. Cheben, A. Ortega-Moñux, R. Halir, Í. Molina-Fernández, *Opt. Laser Technol.* **2019**, *109*, 437.
[5] A. Torres-Cubillo, J. M. Luque-González, A. Sánchez-Postigo, A. Fernández-Gavela, J. G. Wangüemert-Pérez, I. Molina-Fernández, R. Halir, *J. Lightwave Technol.* **2023**, 1.
[6] E. A. Rank, S. Nevlacsil, P. Muellner, R. Hainberger, M. Salas, S. Gloor, M. Duelk, M. Sagmeister, J. Kraft, R. A. Leitgeb, W. Drexler, *Sci. Rep.* **2021**, *11*, 21052.
[7] C. Rogers, A. Y. Piggott, D. J. Thomson, R. F. Wiser, I. E. Opris, S. A. Fortune, A. J. Compston, A. Gondarenko, F. Meng, X. Chen, G. T. Reed, R. Nicolaescu, *Nature* **2021**, *590*, 256.
[8] C. V. Poulton, M. J. Byrd, P. Russo, B. Moss, O. Shatrovoy, M. Khandaker, M. R. Watts, *IEEE J. Sel. Top. Quantum Electron.* **2022**, *28*, 5.
[9] A. Isichenko, N. Chauhan, D. Bose, J. Wang, P. D. Kunz, D. J. Blumenthal, *Nat. Commun.* **2023**, *14*, 3080.
[10] P. Cheben, J. H. Schmid, S. Wang, D.-X. Xu, M. Vachon, S. Janz, J. Lapointe, Y. Painchaud, M.-J. Picard, *Opt. Express* **2015**, *23*, 22553.
[11] D. Vermeulen, C. V. Poulton, *Proc. IEEE* **2018**, *106*, 2270.
[12] C.-S. Im, B. Bhandari, K.-P. Lee, S.-M. Kim, M.-C. Oh, S.-S. Lee, *Opt. Express* **2020**, *28*, 3270.
[13] P. Ginel-Moreno, A. Hadij-ElHouati, A. Sánchez-Postigo, J. G. Wangüemert-Pérez, I. Molina-Fernández, J. H. Schmid, P. Cheben, A. Ortega-Moñux, *Laser Photonics Rev.* **2022**, *16*, 2200164.
[14] J. Riemensberger, A. Lukashchuk, M. Karpov, W. Weng, E. Lucas, J. Liu, T. J. Kippenberg, *Nature* **2020**, *581*, 164.
[15] Y. Li, L. Marais, H. Khettab, Z. Quan, S. Aasmul, R. Leinders, R. Schüler, P. E. Morrissey, S. Greenwald, P. Segers, et al., *Biomed. Opt. Express* **2020**, *11*, 3913.
[16] H. Li, W. Zhou, M. Zhang, Y. Liu, C. Zhang, E. Li, C. Miao, C. Tang, et al., *Sci. World J. 2014*, **2014**, 586517.
[17] S. Kim, D. A. Westly, B. J. Roxworthy, Q. Li, A. Yulaev, K. Srinivasan, V. A. Aksyuk, *Light: Sci. Appl.* **2018**, *7*, 1.
[18] J. Trisno, T. H. Lee, P. N. S., Y. S. Tan, R. J. H. Ng, Y. Huang, S. T. Ho, J. K. W. Yang, *arXiv* **2020**.
[19] C. Ropp, A. Yulaev, D. Westly, G. Simelgor, V. Aksyuk, *Opt. Express* **2021**, *29*, 14789.
[20] A. Yulaev, S. Kim, Q. Li, D. A. Westly, B. J. Roxworthy, K. Srinivasan, V. A. Aksyuk, *Nat. Nanotechnol.* **2022**, *17*, 583.
[21] Y. Livneh, A. Yaacobi, M. Orenstein, *Opt. Express* **2022**, *30*, 8425.
[22] C. Ropp, D. Maurya, A. Yulaev, D. Westly, G. Simelgor, V. Aksyuk, *Opt. Express* **2023**, *31*, 40792.
[23] H. Huang, A. C. Overvig, Y. Xu, S. C. Malek, C.-C. Tsai, A. Alù, N. Yu, *Nat. Nanotechnol.* **2023**, *18*, 580.
[24] A. Yulaev, D. A. Westly, V. A. Aksyuk, *ACS Photonics* **2023**, *10*, 945.
[25] A. Hadij-ElHouati, P. Cheben, A. Ortega-Moñux, J. G. Wangüemert-Pérez, R. Halir, J. de Oliva-Rubio, J. H. Schmid, I. Molina-Fernández, *Opt. Lett.* **2021**, *46*, 2409.
[26] J. M. Luque-González, A. Sánchez-Postigo, A. Hadij-ElHouati, A. Ortega-Moñux, J. G. Wangüemert-Pérez, J. H. Schmid, P. Cheben, Í. Molina-Fernández, R. Halir, *Nanophotonics* **2021**, *10*, 2765.
[27] P. Cheben, J. H. Schmid, R. Halir, J. M. Luque-González, J. G. Wangüemert-Pérez, D. Melati, C. Alonso-Ramos, *Adv. Opt. Photonics* **2023**, *15*, 1033.
[28] T. Tamir, S. T. Peng, *Appl. Phys.* **1977**, *14*, 235.
[29] L. Zavargo-Peche, A. Ortega-Monux, J. G. Wanguemert-Perez, I. Molina-Fernandez, *Prog. Electromagn. Res.* **2012**, *123*, 447.
[30] P. Ginel-Moreno, *Surface-Emitting Antennas for Optical Phased Arrays Based on Silicon Waveguides*, UMA Editorial, **2023**.
[31] W. Fuscaldo, D. R. Jackson, A. Galli, *IEEE Trans. Antennas Propag.* **2017**, *65*, 1670.
[32] Applied Nanotools Inc., Applied Nanotools NanoSOI Fabrication Service, https://www.appliednt.com/nanosoi-fabrication-service/, accessed 06/21/2023.